

Monitoring of underground construction

Stress-path and piezometric head field analysis of soil during earth pressure balanced shield tunneling

A. Afshani & H. Akagi

Waseda University, Tokyo, Japan

ABSTRACT: The effects of earth pressure balanced (EPB) tunneling on the soil stress path and piezometric head of the soil during tunnel advancement are considered in this study. First, the 3D stress distributions of the area near the crown and spring line of the tunnel are investigated, after which the tunnel stress path with respect to the Mohr–Coulomb yielding surface is presented. Next, by taking into account the three significant factors of a) advance rate of the tunnel face, b) consolidation coefficient of the soil, and c) overburden depth of the tunnel, a parametric study is conducted and the effect of EPB tunneling on the piezometric head field of the soil is examined.

1 INTRODUCTION

The prediction of the tunnel-induced soil deformation which arises from the changes of the in situ soil stress and pore water pressure represents a major factor in the design of the tunnels. In this way, the complexity of the mechanism which causes ground movement has encouraged widespread use of numerical analyses since early 1980s in tunnel engineering.

The first finite element models (FEMs) developed for simulation of shield tunneling were proposed in two-dimensional (2D) formats (Finno & Clough 1985), and then in the early 1990s in the form of 2D combination of plane strain ‘transverse-longitudinal’ section (Abu-Farsakh & Voyiadjis 1999, Lee & Rowe 1990). Later on, three-dimensional (3D) finite element (FE) analysis were compared with 2D analysis of plane strain condition, and it was concluded that for elasto-plastic analyses, the stress path in 2D FE analysis would have satisfied the yield condition, whereas that in 3D analysis remains in the elastic regime owing to drainage from the tunnel face (Ohtsu et al. 1999). Ohtsu and collaborators demonstrated that the change in pore water pressure and effective stress varies greatly according to the permeability of the ground and advance rate of the tunnel face. Considering the influence of previous stress history and stress path direction during tunneling, Potts and collaborators studied the ground surface settlement trough induced by tunneling and concluded that a more realistic undrained settlement trough induced by tunneling can be simulated if the effect of previous stress history is taken into account (Grammatikopoulou et al. 2008). By the use of two numerical codes of FLAC and Phase, Cai (2008) simulated a tunnel excavation problem by representing related soil stress paths. He concluded that stress path changes in tunnel not only exist over a long time span such as tunnel face advancing but also show up in a

very short time span such as “instant” removing of a rock block.

This study deals with the effect of earth pressure balanced (EPB) tunneling on the soil stress path and also piezometric head of the soil during tunnel advancement. The content includes two main parts.

First, the effect of EPB shield tunneling on the soil stress path is investigated. Using the elastic perfectly plastic constitutive model with Mohr–Coulomb failure criterion, the 3D stress distribution and soil stress path surface is investigated.

Next, taking into account the three significant factors of a) advance rate of the tunnel face, b) consolidation coefficient of the soil, and c) overburden depth of the tunnel, a parametric study is conducted, and the effect of EPB tunneling on the piezometric head field of the soil is examined.

2 EPB SHIELD TUNNELING EFFECT ON SOIL STRESS PATH

2.1 General

In this section, the soil stress path during EPB shield tunnel advancement is investigated. By using the elastic perfectly plastic constitutive model with Mohr–Coulomb failure criterion, the 3D stress distribution of the area near the crown and spring line of the tunnel due to EPB shield construction is presented, after which the stress path with respect to the M–C yielding surface is drawn.

2.2 Numerical model and its parameters

To generate the tunnel stress path during TBM face advancement, a 3D model was created by numerical code PLAXIS 3D.

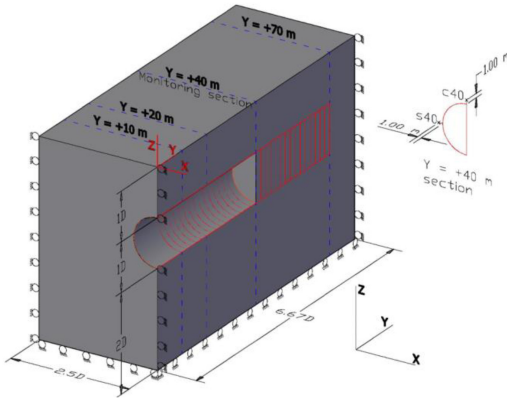


Figure 1. Numerical model used in PLAXIS.

A tunnel of diameter D in a uniform soil deposit with an overall thickness of $4D$, a width of $2.5D$, and a length of $6.67D$ is assumed. The 3D model and its boundaries are shown in Figure 1. Numerical analyses were performed for a tunnel (with an outside diameter of $D = 12$ m) that advances in the y -direction for 25 steps (from $y = +20$ m to $y = +70$ m in Figure 1). On each step, the tunnel face moves forward by $\Delta y = +2$ m. The length of the TBM is assumed to be 10 m, and lies from $y = +10$ m to $y = +20$ m before the start of the first step. The tunnel is assumed to be excavated by the EPB shield method. As the TBM advances, a monitoring section ($y = +40$ m) is considered for measurement purposes mid-way into the tunnel path, as shown in Figure 1.

The tunnel lining is assumed to be 30 cm thick, and is placed immediately following the next round of advancement.

The Mohr–Coulomb constitutive model with a drained condition is used for soil modeling. The water table is 4 m below ground level at $z = -4$ m. Table 1 lists the properties of the soil and concrete lining used in the analyses.

2.3 Stress path analysis

2.3.1 Initial assumptions

To generalize the investigation, three different soil types and three different loading cases were considered, as presented in Tables 2 and 3, respectively. In Table 2, Poisson's ratio, total unit weight, friction angle, and permeability of the soil are taken to be constant for the three soil types. The values listed in Table 2 cover a wide range of soils that may be encountered in urban tunneling, from hard clay and very dense sand (Type 1) to very soft clay and loose sand (Type 3), although rock material is excluded.

Regarding the face pressure in the case of EPB tunneling, the chamber pressure at the excavation face is generally controlled within a range between the active earth pressure and the earth pressure at rest; otherwise,

Table 1. Properties of soil and concrete lining.

Soil parameters used for stress path investigation	Value	Unit
Young's modulus (E_s) ¹	10, 30, 200	MN/m ²
Poisson's ratio (ν_s)	0.35	–
Total unit weight (γ_t)	19.5	kN/m ³
Cohesion (c) ¹	10, 20, 100	kN/m ²
Friction angle (φ)	30	°
Permeability (k)	8.64×10^{-4}	m/day
Soil parameters used for piezometric head field analysis		
Young's modulus (E_s)	298	MN/m ²
Poisson's ratio (ν_s)	0.3	–
Total unit weight (γ_t)	19.5	kN/m ³
Cohesion (c)	60	kN/m ²
Friction angle (φ)	30	°
Permeability (k) ²	8.64×10^{-4} , 8.64×10^{-3} , 8.64×10^{-2} , 8.64×10^{-1} , $8.64 \times 10^{+1}$	m/day
Lining parameters		
Young's modulus (E_l)	26.1	GN/m ²
Poisson's ratio (ν_l)	0.1	–
Total unit weight (γ_l)	27	kN/m ³

¹Three different values of elastic modulus and cohesion were taken for three soil types assumed in section 2 according to Table 2.

²Five different values of permeability were taken for parametric study of soil coefficient of consolidation in section 3.3.

ground settlement or heave occurs (Qu et al. 2009). As the maximum case, passive earth pressure is also taken into consideration.

The loading case values listed in Table 3 for face pressure are obtained by considering the active, at rest, and passive earth pressures as well as the hydrostatic pressure in the tunnel crown at $z = -12$ m, and in the tunnel invert at $z = -24$ m. The face pressure acts perpendicularly to the tunnel face and increases with depth according to the rates of increment presented in Table 3. The potential upper bound for the tail void grouting pressure is also the overburden pressure at the tunnel crown (Thompson et al. 2008).

Therefore, in the three loading cases, values of the tail grouting pressure were assumed to be constant and equal to the ground overburden pressure values at the tunnel crown and invert. The grouting pressure is applied radially and increases with depth according to the values listed in Table 3.

In Table 3, the coefficients of active, at rest, and passive earth pressures were set to 0.33, 0.5, and 3, respectively, by assuming $\phi = 30^\circ$ and by using Jaky's equation and Rankine theory.

In total, for each soil type listed in Table 2, along with each loading case listed in Table 3, numerical analyses were conducted for nine cases.

Table 2. Soil types assumed for stress path analyses during EPB tunneling.

Soil types	Young's modulus (E_s), MN/m ²	Poisson's ratio (ν_s)	Total unit weight (γ_t), kN/m ³	Cohesion (c), kN/m ²	Friction angle (φ), °	Permeability (k), m/day
Type 1	200	0.35	19.5	100	30	8.64×10^{-4}
Type 2	30	0.35	19.5	20	30	8.64×10^{-4}
Type 3	10	0.35	19.5	10	30	8.64×10^{-4}

Table 3. Loading cases for face support and tail grouting pressure assumed for stress path investigations.

Loading case	Face pressure	Tail grouting pressure
Active	128 kPa at tunnel crown ($z = -12$ m), and increase with 13.1 kPa/m in depth	226 kPa at tunnel crown ($z = -12$ m), and increase with 19.5 kPa/m in depth.
At rest	153 kPa at tunnel crown ($z = -12$ m), and increase with 14.75 kPa/m in depth	226 kPa at tunnel crown ($z = -12$ m), and increase with 19.5 kPa/m in depth
Passive	517 kPa at tunnel crown ($z = -12$ m), and increase with 38.5 kPa/m in depth	226 kPa at tunnel crown ($z = -12$ m), and increase with 19.5 kPa/m in depth

2.3.2 Monitoring points for analysis

In Figure 1, two monitoring points were considered on the spring line and crown of the tunnel at $y = +40$ m section as follows.

- (i) s40: a point one meter away from the tunnel spring line in the horizontal direction at $y = +40$ m.
- (ii) c40: a point one meter away from the tunnel crown in the vertical direction at $y = +40$ m.

The principal effective stress values at points s40 and c40 were obtained throughout tunnel advancement, after which the stress paths were plotted for the nine analysis cases.

2.3.3 2D chart of stress path

Chen and Tseng proposed a 2D tunneling chart obtained from redistributed 3D principal stress paths for the Mohr–Coulomb failure criterion and mapped all deviatoric planes into a unique normalized deviatoric plane in which the stress path could be easily traced (Chen & Tseng 2010). By using the proposed tunneling chart and the Mohr–Coulomb failure criterion, the soil stress paths of the monitoring points during tunneling were obtained.

The 2D tunneling chart method used here, proposed by Chen and Tseng, is described in section 2.3.4

Figures 2 and 3 show the variations in the effective principal stress at points c40 and s40 of the monitoring section during TBM face advancement for soil type 1 in the case of active loading. In Figure 2, the effective principal stress (σ'_1) at c40 decreases and converges with the two other effective stresses as the tunnel face approaches the monitoring section at $y = +40$ m. In Figure 3, the effective principal stresses undergo a gradual increase as the tunnel face approaches and passes the monitoring section. A small increase due to

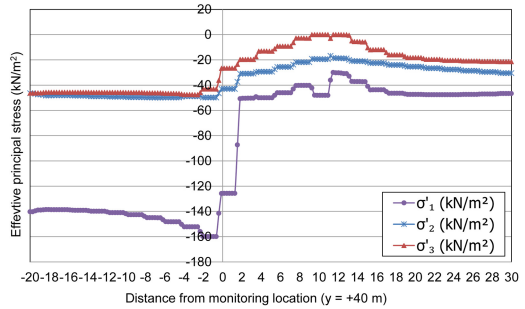


Figure 2. Effective principal stress variation at point c40 for soil type 1 during active loading.

tail void grouting is also noticeable 10 m after passing the monitoring section.

By using the 2D tunneling chart method, the normalized deviatoric stress paths at points c40 and s40 for soil type 1 in the case of active loading are also shown in Figures 4 and 5, respectively. As these figures show, the tunnel stress paths are inside the yielding surface during TBM advancement.

In Figure 4, as the TBM face approaches the monitoring location, the stress path moves away from the yielding surface. This is because according to Figure 2, stress component values tend to converge, whereas in the case of Figure 5, the difference between principal stress component values tend to be constant, which is the reason for the concentrated shape of the stress path at point s40. Among the nine analysis cases, the stress path of low-strength soil type 3 during high-intensity passive loading is assumed to be the most likely to touch or cross the yielding surface.

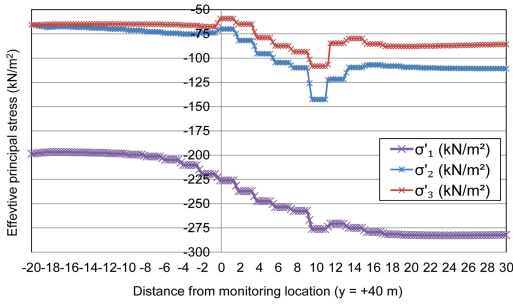


Figure 3. Effective principal stress variation at point s40 for soil type 1 during active loading.

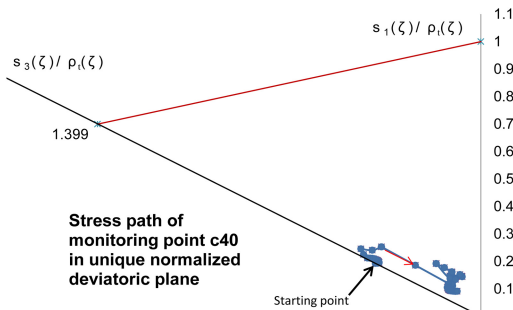


Figure 4. Stress path of point c40 in unique normalized deviatoric plane for soil type 1 during active loading.

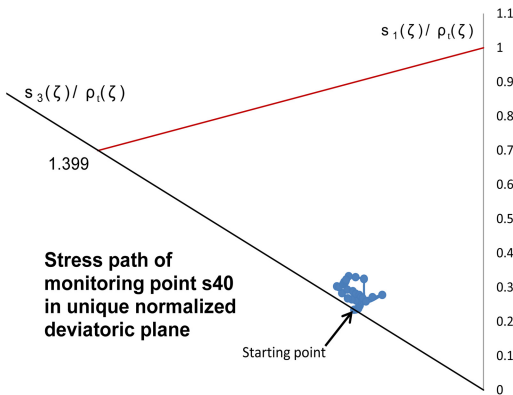


Figure 5. Stress path of point s40 in unique normalized deviatoric plane for soil type 1 during active loading.

Figure 6 and 7 present the normalized deviatoric stress paths of points c40 and s40 for soil type 3 in the case of passive loading. These figures show that the stress paths shift toward the yielding surface, although they are still inside the yielding curve. This means that the stress–strain behavior of the soil is still in the elastic condition for this case (soil type 3 and passive loading).

For all other soil types and loading cases, the stress paths drawn in a similar way were inside the yielding

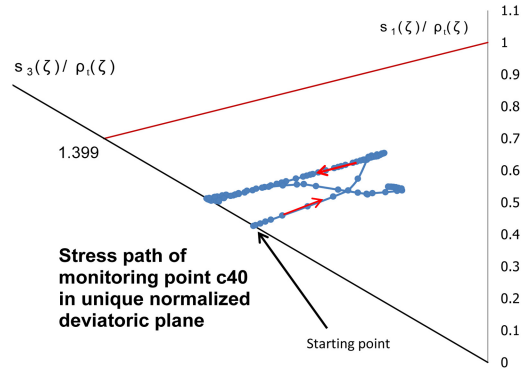


Figure 6. Stress path of point c40 in unique normalized deviatoric plane for soil type 3 during passive loading.

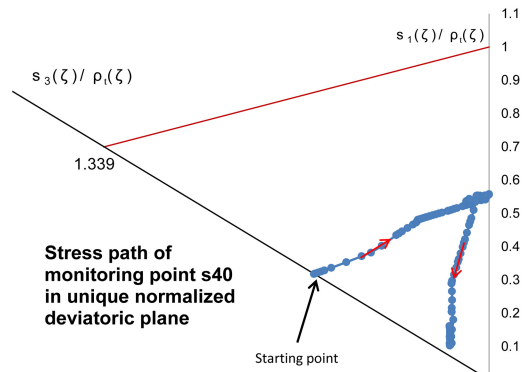


Figure 7. Stress path of point s40 in unique normalized deviatoric plane for soil type 3 during passive loading.

surface. According to the figures presented in this section, in the case of EPB shield tunneling, where efforts are made to maintain the face pressure as close as possible to in situ earth and hydraulic pressure, the soil ahead of the cutter head is in the elastic domain.

Therefore, the results of these analyses display that the stress path of the soil is still inside the yielding surface, and the soil is assumed to be in the elastic zone.

2.3.4 Derivation of normalized deviatoric plane

Based on the Haigh–Westergaard principal stress space (ξ, ρ_0, θ) , the Mohr–Coulomb failure criterion can be presented as (Desai & Siriwardane 1984),

$$f(\xi, \rho_0, \theta) = \sqrt{2}\xi \sin \phi + \sqrt{3}\rho_0 \sin\left(\theta + \frac{\pi}{3}\right) + \rho_0 \cos\left(\theta + \frac{\pi}{3}\right) \sin \phi - \sqrt{6}c \cos \phi = 0 \quad (1)$$

where ξ lies on the hydrostatic axis within the deviatoric plane, as shown in Figure 8a. ρ_0 and θ lie within the deviatoric plane away from the hydrostatic axis in stress space. The associated angle formed with the

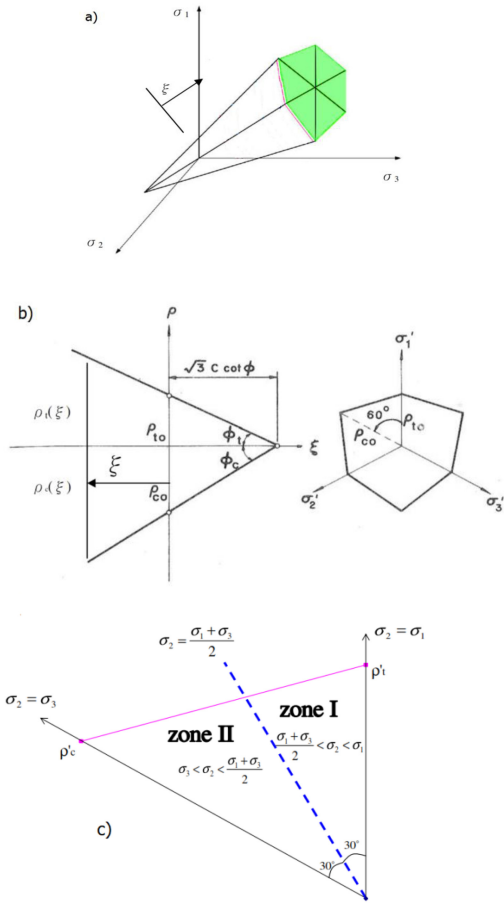


Figure 8. a) Mohr-Coulomb failure criterion; b) π -plane; c) relationship of principal stresses in deviatoric plane.

σ_1 axis is shown in Figure 8b. Three parameters are given as,

$$\xi = \frac{\sigma_1 + \sigma_2 + \sigma_3}{\sqrt{3}} \quad (2)$$

$$\rho_0 = \sqrt{2J_2} \quad (3)$$

$$\cos 3\theta = -\frac{3\sqrt{3} J_3}{2 J_2^{\frac{3}{2}}} \quad (4)$$

where J_2 and J_3 are invariants of the stress deviator tensor given by,

$$J_2 = \frac{1}{3}(I_1^2 - 3I_2) \quad (5)$$

$$J_3 = \frac{1}{27}(2I_1^3 - 9I_1I_2 + 27I_3) \quad (6)$$

$$I_1 = \sigma_1 + \sigma_2 + \sigma_3 \quad (7)$$

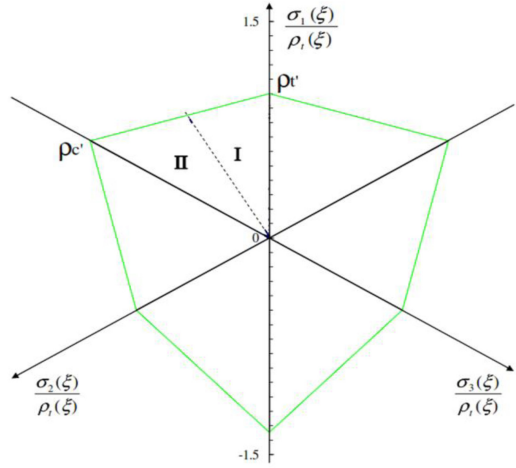


Figure 9. Unique normalized deviatoric plane.

$$I_2 = \sigma_1\sigma_2 + \sigma_2\sigma_3 + \sigma_1\sigma_3 \quad (8)$$

$$I_3 = \sigma_1\sigma_2\sigma_3 \quad (9)$$

In Eq. (1), $\xi = 0$ implies that the hydrostatic pressure is 0, which corresponds to a deviatoric plane (π -plane) that contains the origin. At the π -plane, failure envelopes intersect the σ_1 and $-\sigma_3$ axes at ρ_{c0} and ρ_{t0} , respectively, as shown in Figure 8b; these parameters are defined as follows. The angle of inclination between ρ_{c0} and ρ_{t0} is 60° .

$$\rho_{t0} = \frac{2\sqrt{6}c \cdot \cos \phi}{3 + \sin \phi} \quad (10)$$

$$\rho_{c0} = \frac{2\sqrt{6}c \cdot \cos \phi}{3 - \sin \phi} \quad (11)$$

To obtain the normalized deviatoric plane, $\sigma_1(\xi)$ and $\sigma_3(\xi)$ axes are replaced in the deviatoric planes by the normalized ratios $\sigma_1(\xi)/\rho_t(\xi)$ and $\sigma_3(\xi)/\rho_t(\xi)$, respectively, as illustrated in Figure 9.

The failure envelope intercepts ρ_t along the σ_1 axis, a projection upon the deviatoric plane in the stress space, is normalized to unit length, where $\sigma_1(\xi)/\rho_t(\xi) = \rho_t = 1$.

By using Eqs. (10) and (11), and the friction angle $\phi = 30^\circ$ (refer to Table 1), the normalized length of $\sigma_3(\xi)/\rho_t(\xi) = \rho'_c = 1.399$ along the normalized axis of $\sigma_3(\xi)/\rho_t(\xi)$ is derived. All deviatoric planes corresponding to all loading steps of tunneling can be normalized into one deviatoric plane, which contains the normalized 3D redistributed stress path.

3 EPB SHIELD TUNNELING EFFECTS ON THE PIEZOMETRIC HEAD FIELD

3.1 Piezometric head changes during EPB tunneling

Piezometric head condition of a groundwater during tunneling is a matter that has been discussed mostly in relation to stability of the open tunnel face (Anagnostou 1993, Vermeer et al. 2002).

Factors such as soil type and advance rate of the tunnel face can greatly affect the piezometric head. Pore water pressure generation by application of face pressure and then its dissipation changes the value and direction of the effective principal stresses which subsequently induces soil displacement. Depending on the soil type and advance rate of the tunnel face, soil stress deformation behavior may vary from fully drained to fully undrained condition.

In the following section, three significant factors— a) advance rate of the tunnel face, b) consolidation coefficient of the soil, and c) overburden depth of the tunnel—are considered in conducting a parametric study to investigate the piezometric head changes of the field during EPB shield advancement.

3.2 Method

In EPB tunneling, the tunnel face is supported by excavated soil, water, and additives. At each loading step, face pressure is transmitted to the soil by pressurizing the excavation chamber through the transfer of thrust force into the bulkhead. As the face of the tunnel advances, the excavated soil and water enter the excavation chamber and then are mixed together with additives. Finally, the mixed materials are removed via a screw conveyor and transferred into a conveyor belt, from where it can be transported to the ground surface.

The main assumption here is that the tunnel face is a boundary through which pore water pressure can escape. This means that the excess pore water pressure generated owing to face pressure around the cutter head can be dissipated through the cutter head into the excavation chamber and then out of it through the conveyor belt in the form of muddy soil. At each loading step, for a constant advance rate of the tunnel face ($\Delta x/\Delta t$), TBM moves forward by distance Δx during the time interval Δt .

Figure 10 schematically represents the advance rate of the tunnel face at the first and second loading steps. Immediately after the face pressure acts on the saturated soil, pore water pressure is generated, after which the generated pore pressure starts to dissipate during time interval Δt .

The degree of soil consolidation during this time depends on the advance rate of the tunnel face and the soil type. Pore water pressure values immediately after applying the face pressure and after time Δt can be obtained at the target section in each loading step. The target section, or so-called “monitoring section,” refers to a location where the tunnel-induced displacements

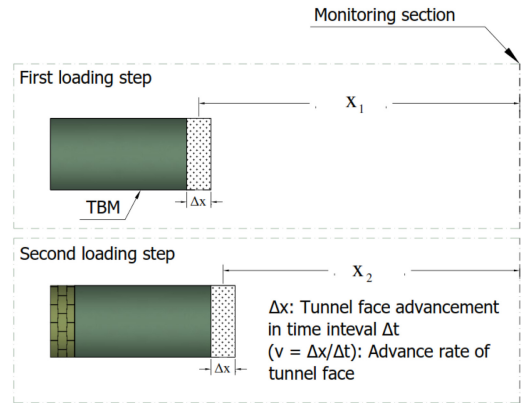


Figure 10. Tunnel face advancement toward monitoring section.

are measured in the field for safety and verification purposes (Fig. 10). Based on Figure 10, for the first loading step, when the average distance of the TBM face from the monitoring section is x_1 , the average excess pore water pressure at the monitoring section immediately after applying face pressure is u_{01} and after time Δt becomes u_1 .

Therefore, the average degree of consolidation at the monitoring section in the first loading step ($x = x_1$), U_1 , can be expressed as

$$U_1 = \frac{u_{01} - u_1}{u_{01}} \times 100(\%) \quad (12)$$

For all other loading steps, similar procedures are taken to evaluate the degree of consolidation. Pore water pressure analysis was carried out using the PLAXIS code by the numerical model introduced in section 2.2. In each loading step, an undrained analysis followed by a consolidation analysis was performed.

3.3 Parametric study

In this section, a parametric analysis is presented to evaluate the influence of three parameters on the piezometric head field in the model introduced in section 2.2.

The parameters are as follows:

- Soil coefficient of consolidation, c_v (m^2/day)
- Advance rate of the tunnel face, v (m/day)
- Overburden depth of the tunnel, H (m)

These parameters are monitored during a 20-m advancement of the TBM from step 1 ($y = +20$ m) to step 10 ($y = +40$ m). During this 10-step advancement, values of excess pore water pressure at the monitoring section ($y = +40$ m) are obtained, and then the average degree of consolidation is calculated at each step by using Eq. (12). The values of the three

Table 4. Values of parameters employed in the parametric study.

Parameters	Values	Unit
Advance rate of tunnel face	1, 2, 5, 10, and 20	m/day
Soil coefficient of consolidation	0.3361, 3.361, 33.61, 336.1, and 33.61×10^3	m^2/day
Overburden depth	12, 18	m

parameters employed in the analyses are listed in Table 4, and the results of the numerical analyses are shown in Figures 11–13. The vertical black lines in these figures display the standard deviations of the degree of consolidation over the tunnel cross section of the monitoring section.

3.4 Influence of soil coefficient of consolidation

To investigate the effect of the soil coefficient of consolidation (c_v), the factor was varied across five values (Table 4). c_v is obtained as follows:

$$c_v = \frac{k}{\gamma_w \cdot \left(\frac{1}{K'} + Q \right)} \quad (13)$$

where γ_w is the unit weight of the pore fluid, k is the coefficient of permeability, K' is the drained bulk modulus of the soil skeleton, and Q represents the compressibility of the fluid.

By neglecting the compressibility of fluid in comparison with soil skeleton, assuming soil bulk modulus value of $K' = 3.89 \times 10^3 \text{ kN/m}^2$, and also five values of coefficient of permeability as $k = 8.64 \times 10^{-4}$, 8.64×10^{-3} , 8.64×10^{-2} , 8.64×10^{-1} , and $8.64 \times 10^{+1} \text{ m/day}$, five values of consolidation coefficient are obtained as shown in Table 4.

In each step, by varying c_v and keeping the two other parameters fixed, the average degree of consolidation is obtained as the tunnel face moves toward the monitoring section.

With two values for the overburden ratio (H) and five values for the advance rate of the tunnel face (v), a total of ten numerical analyses were conducted. Among these cases, one is illustrated in Figure 11. In Figure 11, for example, keeping values of v and H fixed at 1 m/day and 12 m, respectively, the average degree of consolidation is shown for different values of c_v .

The horizontal axis shows the distance of the tunnel face from the monitoring section ($y = +40 \text{ m}$), and the vertical axis represents the average degree of consolidation value according to Eq. (1).

In Figure 11, the average degree of consolidation increases as the tunnel face approaches the monitoring section for all values of c_v . This increase occurs when the tunnel face is closer to the monitoring section for soil cases with lower values of c_v .

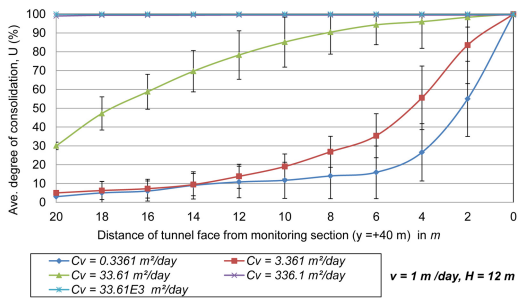


Figure 11. Average degree of consolidation at monitoring section ($y = +40 \text{ m}$) assuming $v = 1 \text{ m/day}$, $H = 12 \text{ m}$.

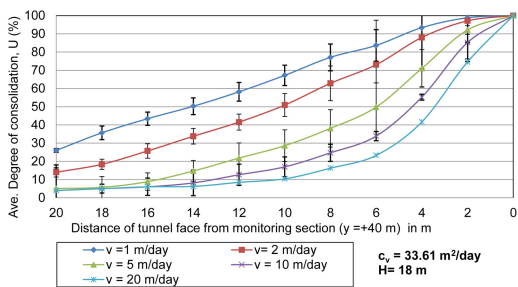


Figure 12. Average degree of consolidation at monitoring section ($y = +40 \text{ m}$) assuming $c_v = 33.61 \text{ m}^2/\text{day}$, $H = 18 \text{ m}$.

On the other hand, in the case of high c_v values, say $c_v = 33.61 \times 10^3 \text{ m}^2/\text{day}$, the generated excess pore water pressure at the monitoring section dissipates quickly regardless of the distance of the tunnel face from the monitoring section (within the range of 20 m), indicating that the drained nature of the soil.

3.5 Influence of advance rate of tunnel face

To examine the influence of the advance rate of the tunnel face, v , the factor was varied across five values of 1, 2, 5, 10, and 20 m/day (Table 4). In Figure 12, for example, v changes while c_v and H were kept constant at $33.61 \text{ m}^2/\text{day}$ and 18 m, respectively.

For the sake of brevity, variations of v with other values of c_v and H other than those in Figure 12 are not shown.

Figure 12 shows that a slower advance rate leads to a higher degree of consolidation at the monitoring section. This is expected because a slower tunnel face implies that more time is available for excess pore water pressure to dissipate.

Figure 12 also shows that v does not influence the dissipation rate of excess pore water pressure as significantly as does c_v while the tunnel face approaches the monitoring section. This issue has also been addressed by Anagnostou (Anagnostou 1993).

3.6 Influence of overburden depth

To investigate the influence of the overburden depth H , two values of 12 and 18 m (1D and 1.5D, where D is the tunnel diameter) were assumed (Table 4).

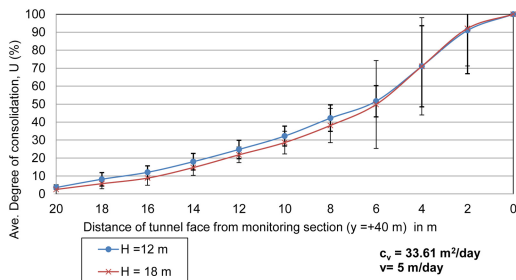


Figure 13. Average degree of consolidation at monitoring section ($y = +40$ m) assuming $c_v = 33.61 \text{ m}^2/\text{day}$, $v = 5 \text{ m/day}$.

This parameter indicates the height of the soil deposit above the tunnel crown.

Figure 13 shows that tunnel excavation at a greater depth slightly decreases the rate of excess pore water pressure dissipation at the monitoring section owing to the longer drainage path, although its effect is far less than that of the two previous parameters. As the tunnel face approaches the monitoring section, the effect of H becomes negligible.

4 CONCLUSION

In this study, the effects of EPB shield tunneling on the stress path and piezometric head field were considered. The results are summarized as follows:

- 1) In the case of EPB tunneling, the face pressure is kept as close as possible to the sum of the in situ soil and hydraulic pressures. Here, by conducting stress path analyses with three soil types under three types of face pressure conditions (active, at rest, and passive load cases), the soil ahead of the tunnel face in EPB tunneling was found to be in the elastic domain.
- 2) To investigate the effects of EPB tunneling on the piezometric head field, a parametric study of the soil coefficient of consolidation, advance rate of tunnel face, and overburden depth was conducted.

In the case of high coefficient of permeability, generated excess pore water pressure dissipates quickly which denotes the drained behavior of soil.

Slower advance rate leads to higher degree of consolidation at the monitoring section.

Excavation at greater depth decreases the rate of excess pore water pressure dissipation at monitoring section slightly due to the longer drainage path.

REFERENCES

- Abu-Farsakh, M. Y., Voyiadjis, G. Z. 1999, Computational model for the simulation of the shield tunneling process in cohesive soils, *International Journal for Numerical and Analytical Methods in Geomechanics*, Vol. 23, No. 1, pp. 23–44.
- Anagnostou, G. 1993, Modelling seepage flow during tunnel excavation, *International Symposium-EUROCK 93*.
- Cai, M. 2008, Influence of stress path on tunnel excavation response numerical tool selection and modeling strategy, *Journal of Tunneling and Underground Space Technology*, Vol. 23, No. 6, pp. 618–28.
- Chen, C. N., and Tseng, C. T. 2010, 2D tunneling chart from redistributed 3D principal stress path, *Tunneling and Underground Space Technology*, Vol. 25, No. 4, pp. 305–14.
- Desai, C. S., and Siriwardane, H. J. 1984, *Constitutive Laws for Engineering Material with Emphasis on Geologic Materials*, Prentice-Hall, Vol. 11.
- Finno, R. J., Clough, G. W. 1985, Evaluation of soil response to EPB shield tunneling, *Journal of Geotechnical Engineering*, Vol. 111, No. 2, pp. 155–73.
- Grammatikopoulou, A., Zdravkovic, L. and Potts, D. M. 2008, The influence of previous stress history and stress path direction on the surface settlement trough induced by tunneling, *Geotechnique Journal*, Vol. 58, No. 4, pp. 269–281.
- Lee, K. M, Rowe, R. K. 1990, Finite element modelling of the three-dimensional ground deformations due to tunneling in soft cohesive soils: part I – method of analysis, *Computers and Geotechnics*, Vol. 10, No. 2, pp. 87–109.
- Ohtsu, H., Ohnishi, Y., Taki, H., and Kamemura, K. 1999, A study on problems associated with finite element excavation analysis by the stress-flow coupled method, *International Journal for Numerical and Analytical Methods in Geomechanics*, Vol. 23, No. 13, pp. 1473–1492.
- Qu, F., Wu, L., and Sun, W. 2009, Analysis of chamber pressure for earth pressure balance shield machine by discrete numerical model, *Intelligent Robotics and Applications*, Springer, pp. 402–411.
- Thompson, J., Chai, J., Biggart, A., and Young, D. 2008, *Earth Pressure Balance Machines for the Silicon Valley Rapid Transit Project—Basis of Design*, North American Tunneling Proceedings, pp. 168–176.
- Vermeer, P. A, Ruse, N. and Marcher, T. 2002, Tunnel heading stability in drained ground, *Felsbau*, Vol. 20, No. 6, pp. 8–18.